Far East J. Appl. Math. **23**(3) (2006), 265-286

LINEAR STABILITY ANALYSIS AND NUMERICAL EXPERIMENTS FOR THREE-DIMENSIONAL NATURAL CONVECTION IN HORIZONTAL ANNULI

ERIC CHÉNIER, GUY LAURIAT and GIUSEPPE PETRONE

University of Marne-la-Vallée
Marne-la-Vallée Cedex 2, France
e-mail: eric.chenier@univ-mlv.fr
guy.lauriat@univ-mlv.fr

Abstract

Natural convection in air-filled horizontal annuli is studied numerically for radius ratio and Rayleigh number in the ranges $1.2 \le R \le 3$ and $Ra < 150{,}000$. Three complementary approaches are used to investigate stability and multiplicity of flow states. A systematic investigation performed for two-dimensional flows leads first to establish a stability diagram of flow regimes as a function of Ra and R. Flow transitions as a function of R, from narrow to large gap annuli of infinite length, are then examined by using 3D-linear stability computations. New stable and unstable regions are highlighted and are strengthened thanks to direct 3D-numerical experiments for finite length annuli. The influences of both the axial aspect ratio on the onset of instabilities and the initial conditions on the asymptotic flow states are also examined.

www.spbni.com

I. Introduction

Free convection in horizontal annuli bounded by two cylinders held at different temperatures has been intensely studied in the last past

2000 Mathematics Subject Classification: 76D05, 76E06, 76M12.

Keywords and phrases: natural convection, horizontal annulus, Boussinesq approximation.

Received March 1, 2006

© 2006 Pushpa Publishing House

decades from the experimental, numerical and theoretical points of view. Besides the technological applications such as thermal storage systems, this geometrical configuration offers a large variety of flow patterns because it consists in four regions over which the thermal gradient rotates between horizontal and vertical directions. In addition, a rich diversity of natural convective flows occurs according to the Rayleigh and Prandtl number values, Ra and Pr, but also according to the values of the annulus length and radius ratio of the cylinders, R, which is a key dimensionless parameter.

Although the first studies on natural convection in horizontal annuli probably date from the 30's [1], the first relevant analyses for the flow properties come from the experimental works by Bishop et al. [2, 3], Grigull and Hauf [15] and Powe et al. [28] who established the famous chart summing up the flow regime and the spatial patterns for air-filled annuli as a function of the Grashof number and radius ratio.

For small Rayleigh numbers, the flow consists in a two-dimensional crescent-shaped flow formed by two large cells, symmetrically located with respect to the vertical plane containing the cylinder axes. For wide gap annuli, i.e., for radius ratio larger than $R = 1.71$ [28], the fluid particle trajectories lie mainly in the cross-section of the annulus with a very small axial dependency. This flow pattern was termed helical. The transition therefore happens for large Ra-values from an almost two-dimensional steady flow to an oscillatory flow, as observed in experiments [2, 3, 18]. For moderate gap annuli ($1.24 < R < 1.71$ [28]) and past the transition, a three-dimensional spiral flow is observed, resulting from the combination of two origins of the fluid motion: in the lower region of the annulus, the helical structure persists whereas counter-rotating transverse rolls (with respect to the annulus axis) develop in the upper part of the annular space. The onset of transverse rolls at the top of the annuli was confirmed by linear stability analysis and by three-dimensional numerical simulations [8, 11, 15, 30]. For narrow gap annuli ($R < 1.24$ [28]), the basic crescent-shaped flow evolves towards multi-cellular flows giving birth to longitudinal rolls at the top of the annular space. The changes in the flow patterns were

www.nphmj.com

widely studied numerically by performing two-dimensional computations for flows assumed to only occur in the cross-section of the annular spaces [4-6, 9, 10, 20, 21, 29, 31, 32]. It was shown that the slight curvature of the cylinder walls at the top of the annular space breaks the usual Rayleigh-Bénard pitchfork bifurcation into a couple of a *virtual transcritical* bifurcation and a saddle-node bifurcation. Therefore, two branches of solutions, disconnected from each other, exist above a threshold Rayleigh number. According as the flow belongs to one or to the other branch, the solution exhibits a different number of counter-rotating cells at the top of the annulus for the same set of parameter values. Contrary to the Powe chart [28] and the two-dimensional simulations describing transitions to longitudinal rolls at the top of narrow gap annuli, the three-dimensional stability analyses [8, 11, 23], confirmed by three-dimensional simulations [11], foresee the growing of transverse rolls at the top of the annulus, like for moderate radius ratios. However for $R \leq 1.2$, three-dimensional numerical simulations performed by Dyko and Vafai [13] have shown possible combinations between transverse and longitudinal rolls in the upper region of the annulus. In that case, the longitudinal patterns look like those predicted by two-dimensional simulations and shown in the Powe chart [28].

The purpose of this article is to present up to date numerical solutions and linear stability analysis results for natural convection between differentially heated horizontal cylinders. A special attention is brought on flow patterns and flow stability properties. In what follows, the paper is divided into three main parts. The problem and the equations are first established for the fluid motion and for the linear stability analysis. The discrete models and numerical methods are then introduced. The results are presented into three sub-sections. First, a review of the fluid flow occurring in the transverse section of an annular space is discussed with a particular interest put on the multiplicity of solutions for a fixed set of parameters. A chart summing up the flow patterns is then established for large ranges of Rayleigh number and radius ratio values. In the second sub-section, three-dimensional linear stability analyses of these flows are then led, complementing the studies reported in the current literature for moderate and large radius ratios.

www.pphmj.com

The reason of the sudden disappearance of the Ra-threshold value for $R \geq 2$ is clearly shown. In the last sub-section, the discussion is on three-dimensional simulations carried-out to validate the stability diagram and to describe the fluid motions in the instability regions of two-dimensional flows. The effects of the axial aspect ratio and of the initial conditions on the onset of the amplification of instabilities are investigated.

II. Continuous Models

A. Governing equations

The annulus of length L^* is formed by two co-axial cylinders of radii $r_i^* < r_o^*$, held at uniform temperatures $T^*(r_i^*) = T_i^* > T^*(r_o^*) = T_o^*$ and bounded by two impermeable and adiabatic plates (Figure 1). The flow is assumed to be laminar and incompressible with constant physical properties except the density in formulating the buoyancy effect (Boussinesq approximation). By scaling the axial coordinate by the annulus gap $d^* = r_o^* - r_i^*$, the velocity components by the thermal diffusivity velocity α/d^*, by introducing the dimensionless temperature difference $T = (T^* - T_r^*)/(T_i^* - T_o^*)$, where $T_r^* = (T_i^* + T_o^*)/2$ is the reference temperature, and the dimensionless radial coordinate $r = (r^* - r_i^*)/d^*$, the dimensionless governing equations write in cylindrical coordinates (r, θ, z):

$$\bar{\bar{\nabla}} \cdot \vec{V} = 0, \tag{1a}$$

$$\frac{\partial}{\partial t}(fu) + \bar{\bar{\nabla}} \cdot (u\vec{V}) - \eta v^2 = -f \frac{\partial p}{\partial r} - RaPrf\, T \cos\theta + Pr\left(\tilde{\nabla}^2 u - \frac{2\eta^2}{f}\frac{\partial v}{\partial \theta} - \frac{\eta^2 u}{f}\right), \tag{1b}$$

$$\frac{\partial}{\partial t}(fv) + \bar{\bar{\nabla}} \cdot (v\vec{V}) + \eta uv = -\eta \frac{\partial p}{\partial \theta} + RaPrf\, T \sin\theta + Pr\left(\tilde{\nabla}^2 v + \frac{2\eta^2}{f}\frac{\partial u}{\partial \theta} - \frac{\eta^2 v}{f}\right), \tag{1c}$$

www.pnrmj.com

$$\frac{\partial}{\partial t}(fw) + \tilde{\nabla} \cdot (w\vec{V}) = -f\frac{\partial p}{\partial z} + Pr\tilde{\nabla}^2 w, \tag{1d}$$

$$\frac{\partial}{\partial t}(fT) + \tilde{\nabla} \cdot (T\vec{V}) = \tilde{\nabla}^2 T, \tag{1e}$$

where $\eta = r_o^*/r_i^* - 1$ and $f = \eta r + 1$. The spatial operators are defined as follows:

$$\tilde{\nabla} \cdot (X\vec{V}) = \frac{\partial(fXu)}{\partial r} + \frac{\partial(\eta Xv)}{\partial \theta} + \frac{\partial(fXw)}{\partial z},$$

$$\tilde{\nabla}^2 X = \frac{\partial}{\partial r}\left(f\frac{\partial X}{\partial r}\right) + \frac{\partial}{\partial \theta}\left(\frac{\eta^2}{f}\frac{\partial X}{\partial \theta}\right) + \frac{\partial}{\partial z}\left(f\frac{\partial X}{\partial z}\right),$$

where $X(r, \theta, z)$ is a scalar quantity. The problem is then characterized by four dimensionless parameters: the Prandtl number, $Pr = \nu/\alpha$, the Rayleigh number based on the annulus gap, $Ra = g\beta(T_i^* - T_o^*)d^{*3}/(\nu\alpha)$, the radius ratio, $R = r_o^*/r_i^*$, and the axial aspect ratio, $A = L^*/d^*$. The boundary conditions are

$$u = v = w = 0, \quad T = +0,5 \text{ at } r = 0, \tag{2a}$$

$$u = v = w = 0, \quad T = -0,5 \text{ at } r = 1, \tag{2b}$$

$$u = v = w = 0, \quad \frac{\partial T}{\partial z} = 0 \text{ at } z = 0 \text{ and } z = A. \tag{2c}$$

Owing to the symmetry both of the experimentally observed flows and dominant disturbances computed by stability analyses, the half cross-section annulus is generally considered when computing three-dimensional flows, with the following symmetry conditions applied at $\theta = 0$ and π:

$$\frac{\partial u}{\partial \theta} = 0, \quad v = 0, \quad \frac{\partial w}{\partial \theta} = 0, \quad \frac{\partial T}{\partial \theta} = 0, \text{ at } \theta = 0 \text{ and } \theta = \pi.$$

The two-dimensional base flows introduced when conducting stability analysis are assumed independent of the axial direction. The fluid flow is then governed by equations (1a)-(1c) and (1e) for an axial component of the velocity equal to zero $(w = 0)$, provided with the boundary conditions (2a)-(2b).

www.phhnj.com

The local Nusselt number at any axial location on the cylinder surfaces is defined by

$$Nu(\theta, z) = -ln(R)\left(r_c + \frac{1}{R-1}\right)\frac{\partial T}{\partial r}\bigg|_{r_c},$$

where r_c stands for $r_i = 0$ or $r_o = 1$.

B. Linear stability problem

Consider the two-dimensional steady velocity $\vec{u}_0 = u_0\vec{e}_r + v_0\vec{e}_\theta$, temperature T_0, and pressure p_0 fields and the following three-dimensional disturbances $\delta\vec{u} = \delta u\vec{e}_r + \delta v\vec{e}_\theta + \delta w\vec{e}_z$, δT and δp satisfying slip boundary conditions on the adiabatic end-walls at $z = 0, A$:

$$\begin{cases} \delta u = \overline{u}(r, \theta, t)\cos(kz), \\ \delta v = \overline{v}(r, \theta, t)\cos(kz), \\ \delta w = \overline{w}(r, \theta, t)\sin(kz), \\ \delta p = \overline{p}(r, \theta, t)\cos(kz), \\ \delta T = \overline{T}(r, \theta, t)\cos(kz), \end{cases} \tag{3}$$

where $k = n\pi/A$ is the dimensionless wavenumber and n is an integer. By substituting in the governing equations (1) the velocity, pressure and temperature fields by $\vec{u}_0 + \delta\vec{u}$, $p_0 + \delta p$ and $T_0 + \delta T$ and by neglecting the second-order transport terms, the variables $\overline{u}$, $\overline{v}$, $\overline{w}$, $\overline{p}$ and $\overline{T}$ satisfy the time-dependent equations

$$\frac{\partial(f\overline{u})}{\partial r} + \eta\frac{\partial\overline{v}}{\partial\theta} + fk\overline{w} = 0, \tag{4a}$$

$$\begin{aligned} \frac{\partial(f\overline{u})}{\partial t} = &-\frac{\partial(f\overline{u}u_0)}{\partial r} - \frac{\partial(\eta\overline{v}u_0)}{\partial\theta} - fk\overline{w}u_0 + \eta\overline{v}v_0 \\ &- \frac{\partial(fu_0\overline{u})}{\partial r} - \frac{\partial(\eta v\overline{u})}{\partial\theta} + \eta v_0\overline{v} \\ &- f\frac{\partial\overline{p}}{\partial r} + Pr\left(\frac{\partial}{\partial r}\left[f\frac{\partial\overline{u}}{\partial r}\right] + \frac{\partial}{\partial\theta}\left[\frac{\eta^2}{f}\frac{\partial\overline{u}}{\partial\theta}\right] - fk^2\overline{u} - \frac{2\eta^2}{f}\frac{\partial\overline{v}}{\partial\theta} - \frac{\eta^2\overline{u}}{f}\right) \\ &- RaPrf\overline{T}\sin\theta, \end{aligned} \tag{4b}$$

www.nphmj.com

$$\frac{\partial(f\overline{v})}{\partial t} = -\frac{\partial(f\overline{u}v_0)}{\partial r} - \frac{\partial(\eta\overline{v}v_0)}{\partial\theta} - fk\overline{w}v_0 - \eta\overline{u}v_0$$
$$-\frac{\partial(fu_0\overline{v})}{\partial r} - \frac{\partial(\eta v_0\overline{v})}{\partial\theta} - \eta u_0\overline{v}$$
$$-f\frac{\partial\overline{p}}{\partial\theta} + Pr\left(\frac{\partial}{\partial r}\left[f\frac{\partial\overline{v}}{\partial r}\right] + \frac{\partial}{\partial\theta}\left[\frac{\eta^2}{f}\frac{\partial\overline{v}}{\partial\theta}\right] - fk^2\overline{v} + \frac{2\eta^2}{f}\frac{\partial\overline{u}}{\partial\theta} - \frac{\eta^2\overline{v}}{f}\right)$$
$$+ RaPrf\overline{T}\sin\theta, \tag{4c}$$

$$\frac{\partial(f\overline{w})}{\partial t} = -\frac{\partial(fu_0\overline{w})}{\partial r} - \frac{\partial(\eta v_0\overline{w})}{\partial\theta} + fk\overline{p}$$
$$+ Pr\left(\frac{\partial}{\partial r}\left[f\frac{\partial\overline{w}}{\partial r}\right] + \frac{\partial}{\partial\theta}\left[\frac{\eta^2}{f}\frac{\partial\overline{w}}{\partial\theta}\right] - fk^2\overline{w}\right), \tag{4d}$$

$$\frac{\partial(f\overline{T})}{\partial t} = -\frac{\partial(f\overline{u}T_0)}{\partial r} - \frac{\partial(\eta\overline{v}T_0)}{\partial\theta} - fk\overline{w}T_0 - \frac{\partial(fu_0\overline{T})}{\partial r} - \frac{\partial(\eta v_0\overline{T})}{\partial\theta}$$
$$+ \frac{\partial}{\partial r}\left[f\frac{\partial\overline{T}}{\partial r}\right] + \frac{\partial}{\partial\theta}\left[\frac{\eta^2}{f}\frac{\partial\overline{T}}{\partial\theta}\right] - fk^2\overline{T}. \tag{4e}$$

The boundary conditions for the unknowns $\overline{u}$, $\overline{v}$, $\overline{w}$, and $\overline{T}$ are homogeneous.

III. Discrete Models and Numerical Methods

The numerical scheme and the numerical methods are shortly presented. For more details, refer to references [24, 26, 27].

A. Spatial and temporal discretization

The governing equations with the boundary conditions were solved numerically in the primitive variable formulation by using a finite volume method on a staggered but structured grid. For a half-annulus, the mesh defined by $[r_i, r_{i+1}]\times[\theta_j, \theta_{j+1}]\times[z_k, z_{k+1}]$ was built up as

$$r_i = \frac{\tanh\left(c_r\left(2\frac{i-1}{N_r} - 1\right)\right) + \tanh(c_r)}{2\tanh(c_r)}, \quad i = 1, N_r + 1,$$

www.rphni.com

$$\theta_j = \pi \frac{\exp\left(\pi c_\theta \dfrac{j-1}{N_{\theta_1}}\right) - 1}{\exp(\pi c_\theta) - 1}, \quad j = 1,\ N_{\theta_1} + 1,$$

$$z_k = A \frac{\tanh\left[c_z\left(2\dfrac{k-1}{N_z} - 1\right)\right] + \tanh(c_z)}{2\tanh(c_z)}, \quad k = 1,\ N_z + 1.$$

For the computations of the two-dimensional steady states and the dominant disturbances, the full angular domain was considered

$$\theta_j = \begin{cases} \pi \dfrac{\exp\left(2\pi c_\theta \dfrac{j-1}{N_{\theta_2}}\right) - 1}{\exp(\pi c_\theta) - 1}, & j = 1,\ \dfrac{N_{\theta_2}}{2} + 1, \\ 2\pi - \theta_{N_{\theta_2}+2-j}, & j = \dfrac{N_{\theta_2}}{2} + 1,\ N_{\theta_2} + 1. \end{cases}$$

The variables N_r, N_z, N_{θ_1} are any integers and N_{θ_2} is an even integer. In order to adjust the grid distribution at the upper part of the annulus (near $\theta = \pi$) and in the wall regions, three strictly negative real parameters (c_r, c_θ and c_z) were introduced. If one of these three parameters was zero, the grid distribution was uniform in the corresponding direction.

The transport terms of the momentum and energy equations were discretized by using a second-order centred scheme. The time integration was performed by an implicit second-order Euler scheme for the diffusion terms and an Adams-Bashforth extrapolation scheme for the transport terms. The time splitting methods [14] and [16] were used to uncouple velocity and pressure fields for both the three- and two-dimensional computations.

B. Steady two-dimensional flows

The simulations of two-dimensional steady flows provide the basic solutions that are next perturbed by infinitesimal disturbances in order to establish the transition thresholds. Close to the critical parameter, the growth rate of the disturbances tends to zero, so that the use of a time

www.pphmj.com

marching procedure to compute the basic flow is inefficient. In order to obtain multiple flows, a continuation strategy was applied. It implies the computations of steady solutions lying on unstable branches. The two-dimensional basic flows were thus calculated by solving the steady-conservative equations by using the Newton-Raphson method. To avoid constructing explicitly the Jacobian matrix, coming from the linearization of the non-linear equations about the basic flow, an iterative linear solver was used. This solver requires only the knowledge of the product of the Jacobian matrix by any vector. The evaluation of the residual and of the matrix-vector product, preconditioned by the diffusion operators, was performed by Mamun and Tuckerman [19] method. It consists in using two slightly modified temporal codes based on a first-order time differencing and an implicit evaluation of the viscous and thermal diffusions. The preconditioned residual and the Jacobian-vector product are then simply the differences between two successive solutions of two temporal codes build up with the convective non-linear terms and its linearization about the current approximation of the basic flow, respectively.

C. Stability analysis

Several methods were developed to compute the transition thresholds. For the two-dimensional stability analysis, namely equations (4a)-(4c) and (4e) with $w_0 = 0$ and $k = 0$, the bifurcations were evaluated by solving a large non-linear system consisting in the non-linear equations and their linearized counterparts at the transition. The algorithm used is an extension of method [19] briefly presented in Section III B. The direct computation of the bifurcations is particularly relevant to follow transitions as a function of one parameter, the radius ratio for example. Otherwise, an iterative evaluation of the critical parameter based on the shooting method, was applied: let us assume that the bifurcation parameter is Ra and suppose that two Rayleigh number values $Ra^{(0)}$ and $Ra^{(1)}$ were determined so that the growth rates $\lambda^{(0)}$ and $\lambda^{(1)}$ of the dominant perturbation satisfy $\lambda^{(0)} \times \lambda^{(1)} < 0$. Starting from $i = 0$, the following algorithm converges toward the critical value Ra_c:

www.ijrmj.com

1. $Ra^{(i+2)} = \dfrac{Ra^{(i)} \times \lambda^{(i+1)} + Ra^{(i+1)} \times \lambda^{(i)}}{\lambda^{(i)} + \lambda^{(i+1)}}$.

2. The basic flow and then the growth rate $\lambda^{(i+2)}$ are computed at $Ra^{(i+2)}$.

3. • If $\lambda^{(i+2)}$ is small enough, then $Ra_c \approx Ra^{(i+2)}$, stop.

   • If $\lambda^{(i+2)} \times \lambda^{(i)} < 0$, then $Ra^{(i+3)} = Ra^{(i)}$ else $Ra^{(i+3)} = Ra^{(i+1)}$.

4. $i = i + 2$, go to step (1).

This algorithm was found efficient both for two- and three-dimensional disturbances. For the three-dimensional stability analysis, the eigenvalue problem depends on the wavenumber k. Thus for infinite length annuli, the critical Rayleigh number $Ra_c = \min_k(Ra_c)$ (respectively $Ra_c = \max_k(Ra_c)$) for a destabilizing (respectively stabilizing) transition was computed by a quadratic interpolation based on the nearest threshold values $Ra_c(k)$.

IV. Results

All the computations were performed for a Prandtl number value corresponding to air ($Pr = 0.7$).

A. Two-dimensional flows and stability

1. Narrow gap annuli, $R = 1.2$

For a small Rayleigh number value, $Ra < \approx 2000$, the flow consists in two crescent-shaped cells, symmetrical located with respect to the vertical line containing the axis of the cylinders. In each of the two annular half-spaces, the fluid goes upwards and downwards, respectively along the hot inner and cold outer cylinders. The conduction is the major mode of heat transfer between the differentially heated boundaries of the annulus. As the Rayleigh number is increased, the centre of rotation of the main cells moves upward and a thermal plume starts to form at the upper part of the annulus with an impingement region on the outer

www.pphmj.com

cylinder. The distribution of the thermal fluxes along the inner and outer cylinders shows that the largest part of the heat convected within the annulus is extracted from the lower part of the inner cylinder.

To discuss the changes in the flow patterns, a two-dimensional bifurcation diagram representing the steady radial velocity component $u(0.5, \pi)$ as a function of Ra is drawn in Figure 2. This velocity component indicates the direction of the rotating cells in the upper region of the annulus when the flow is symmetric. Each point of these curves represents a different steady-state flow. The steady solutions lying on the continuous and dashed lines are stable and unstable, respectively. Below $Ra_{s_1}^{l} = 1911$, a couple of crescent-shaped cells is the only possible flow structure. Just above $Ra_{s_1}^{l}$, two new steady solutions are found lying on the unstable branch as shown in the enlargement plotted in Figure 2. For convenience, the branches starting from $Ra = 0$ and $Ra_{s_1}^{l}$ will be called in what follows as the "basic-branch" and "lower-branch", respectively: the quantities expressed on these branches are labeled "b" and "l". The sharp growth of $u(0.5, \pi)$ as well as the appearance of the lower-branch of solutions are Rayleigh-Bénard like thermal instabilities. As described in [21], the slight curvature of the walls for $R = 1.2$ breaks the classical pitchfork bifurcation into a saddle-node bifurcation at $Ra_{s_1}^{l} = 1911$ and, into a virtual bifurcation which looks like a transcritical bifurcation at $Ra_t = 1917$. Contrary to what has been shown in [21], the basic solutions lying on the lower part of the lower-branch for $Ra > Ra_{s_1}^{l}$ remain unstable until $Ra \geq Ra_{f_1}^{(l)} = 2000$, where a subcritical pitchfork bifurcation occurs. Another noticeable difference with [21] concerns the stability of flows lying on the basic branch, that is to say the part of the curve which suddenly grows in the enlargement (Figure 2). Indeed, the basic flow is unstable in the Ra-range $Ra_{f_1}^{b} = 2068 < Ra < Ra_{f_2}^{b} = 2456$. The three pitchfork bifurcations $Ra_{f_1}^{b}$, $Ra_{f_2}^{b}$ and $Ra_{f_1}^{l}$ are associated with dominant disturbances breaking the symmetry of the basic flow.

www.pdfmi.com

The flow patterns are now described on each branch of solutions. The stable solutions being always symmetric with respect to the vertical line containing the cylinder axes, only the flow in one half annulus is presented. The cells rotating in the same direction as the large crescent-cell are noted C^+ or c^+, whether they are stretching out on the entire annulus gap or not. The counter-rotating cells are therefore labelled C^-. For $Ra < Ra_t$, the flow pattern labelled C^+ consists in the previously mentioned couple of crescent-shaped cells. Slightly above Ra_t on the basic branch, a co-rotating cell c^+ grows very fast with Ra but remains confined in the large C^+ cell for $Ra <\approx 2270$ (Figure 3(a)) and, then gives rise to a counter-rotating cell C^- located between them (Figure 3(b)). The Ra-value corresponding to the onset of this three-cellular flow, denoted $C^+C^-C^+$, is in good agreement with previous studies [9, 17]. On the lower part of the continuation curve, a reverse flow (Figure 3(c)) appears just after the saddle-node bifurcation point at $Ra_{s_1}^l$, as indicated by the negative radial velocity $u(0.5, \pi)$ on the enlargement in Figure 2.

2. Radius ratio effect

Increases in R lead to displacements of the bifurcation thresholds and modify the shape of the bifurcation diagram. For example at $R \approx 1.26$, a new stable branch of solutions arises and is from now on named "upper branch" [24]. This upper branch originates from the collision of two branches of solutions. As for the lower branch, the upper branch of solutions exists only above the saddle-node bifurcation point at $Ra_s^{(u)}$. As a consequence of the large modification of the bifurcation diagram, the shape of the solutions lying on the basic-branch is substantially modified: the three-cellular flow $C^+C^-C^+$ is now located on the upper-branch whereas the basic branch is mainly characterized by the mono-cellular flow pattern C^+. On the lower branch, the variation of $Ra_{s_1}^l$ as a function of R is found in good agreement with [21] since the largest relative difference is only 0.25% for $1.2 \le R \le 3$. For $R \ge 1.6$, the threshold of the pitchfork bifurcation $Ra_{f_1}^{(l)}$ increases abruptly with R and then

www.iphmj.com

delimits a bounded region outside of which the flow patterns C^-C^+ are unstable. The flow patterns as a function of the radius ratio and Rayleigh number are summed up in Figure 4. Three, two or only one solution may exist for a given parameter set, with a decreasing number of flow patterns when increasing the radius ratio.

B. Three-dimensional linear stability analysis

For infinite length annuli, the flow stability is ensured when all spectral components k of the disturbances are damped. As already mentioned in [8], the first transition for small and moderate radius ratios, $R < 2$, occurs for the couple of counter-rotation cells C^+. In other words, the two- or three-cellular flows are always unstable with respect to three-dimensional disturbances. Although the results of the two-dimensional analysis could therefore be considered as useless, a recent study [7] showed that such multi-cellular solutions are stable above a critical Péclet number value in the case of fully developed mixed convective flows in horizontal annuli.

The critical Rayleigh number values $Ra_c(R)$ are plotted in Figure 5 as a function of $\sigma = 2r_i^*/d^* = 2/(R-1)$ (bottom abscissa axis) or as a function of R (top abscissa axis). It should be noted that parameter σ was widely used in previous works instead of R. The ranges of the radius ratio and Rayleigh number values where the transitions occur are as follows:

- for $1.2 \le R \le 1.95$, $1734 \le Ra_{c_1} \le 2894$;
- for $1.95 \ge R \ge 1.5$, $3643 \le Ra_{c_2} \le 13{,}540$;
- for $1.5 \le R \le 2.24$, $17{,}130 \le Ra_{c_3} \le 52{,}000$;
- for $2.3 \le R \le 3$, $110{,}040 \le Ra_{c_4} \le 151{,}330$.

For $R < 2$ and $Ra < Ra_{c_1}$, low velocity magnitudes are obtained at the top region of the annulus so that a conductive regime is nearly predicted. For small radius ratios, the cylinder surfaces are almost horizontal at the top of the annular space where a Rayleigh-Bénard like instability occurs. Both the shape of marginal mode and the variation of the critical

www.ppmj.com

Rayleigh Ra_{c_1} as a function of R are in agreement with [8]. The usual conditions for the appearance of this instability, namely a conductive regime for the basic flow between differentially heated horizontal plates, are all the more satisfied since the radius ratio and the velocity magnitude at the top annuli are small. Therefore, the reverse transition at Ra_{c_2} is expected for smaller Ra-values as the radius ratio increases (Figure 5, for $1.5 \le R < 2$). Thus, the disappearance of the first transition Ra_{c_1} close to $R = 2$ is not due to the sudden increase of the critical value [8] but rather to the collapse of the unstable region $Ra_{c_1} < Ra < Ra_{c_2}$. Above Ra_{c_2}, the two-dimensional flow is a new stable. New transitions are also reported for large Rayleigh number values: for moderate and large gap annuli, the onsets of oscillatory modes and steady modes occur at Ra_{c_3} and Ra_{c_4}, respectively [27]. Contrary to the oscillatory marginal disturbances, the steady mode consists in flow patterns which do not exhibit the symmetry property. The Hopf bifurcation at Ra_{c_3} does not agree with the stability analysis reported in [8]. The authors predicted indeed a stable behaviour of the two-dimensional basic flow for $R = 2$ at $Ra \le 100{,}000$ whereas our results show a transition at $Ra_{c_3} = 24{,}621$.

Simple analytical functions were sought to define correlations between the critical Rayleigh numbers and the radius ratios. The critical Rayleigh numbers $Ra_{c_i}(R)$ were thus approximated by

- for $1.2 \le R \le 1.95$, $Ra_1(R) = (1072R - 2398)/(0.7069R - 1.485)$ with $|Ra_{c_1} - Ra_1|/Ra_{c_1} < 1.4\%$;
- for $1.95 \ge R \ge 1.5$, $Ra_2(R) = 10{,}440/(R - 1) - 7300$ with $|Ra_{c_2} - Ra_2|/Ra_{c_2} < 2\%$;
- for $1.5 \le R \le 2.24$, $Ra_3(R) = 52{,}000 - 37{,}400 \times (2.24 - R)^{0.244}$ with $|Ra_{c_3} - Ra_3|/Ra_{c_3} < 4\%$;
- for $2.3 \le R \le 3$, $Ra_4(R) = 59{,}100R - 27{,}300$ with $|Ra_{c_4} - Ra_4|/Ra_{c_4} < 1.4\%$.

www.begellhouse.com

C. Numerical simulations

Many experimental results but few three-dimensional numerical solutions were reported in the literature. The most quoted results are shown in a stability chart (Figure 5) which includes the present three-dimensional simulations. The filled and open symbols correspond to three- and to two-dimensional flows, respectively, while the half-filled circles are for parameter values for which both 2D- and 3D-solutions may be obtained. The stability chart by Powe et al. [28] is also drawn in Figure 5.

For narrow annulus gaps ($R < 1.23$), the stability results [8, 11, 22, 23] and three-dimensional simulations [11, 12] confirm the onset of transverse roll disturbances and thus contradict the Powe chart. However, some complex flows were obtained in [13] that consist in development of both the classical transverse rolls and longitudinal cells that could correspond to the 2D-multicellular flows as described by Powe et al. [28].

The multiple transitions presented in the previous section for moderate radius ratios are not mentioned in the chart by Powe et al. [28], in which only the transition close to Ra_{c_1} was reported. The simulation performed in the first instability region ($Ra_{c_1} \le Ra \le Ra_{c_2}$), for $Ra = 6000$, $R = 1.7$, $A = 6$ and represented by a filled square in Figure 5, is in agreement with the results of Dyko et al. [11] and the spiral flow described in experiments [28]. The flow was found steady and the fluid particles injected in the vertical (r, z) upper section of the annulus follow first a spiral motion in the upper part of the cavity and are then ejected in the core region in which a helical motion is observed (Figure 6).

The investigation of the flow motion above the threshold Ra_{c_2} shows clearly the influence of the initial conditions on the steady-state solutions. The simulations were carried-out for $Ra = 10{,}000$, $R = 1.7$ and $A = 6$ and are symbolized by a half-filled circle in Figure 5. By starting the computations with a quiescent fluid at uniform temperature $T = 0$, the flow remains steady and mainly two-dimensional in the core region of the annulus. Figure 7(a) shows that the isotherms plotted in the

www.pphmj.com

upper vertical (r, z)-plane are almost independent of the axial coordinate, except near the end walls where transverse cells form because of the viscous shear associated with the no-slip boundary condition. The average Nusselt numbers at the mid-axial plane $z = A/2$ differ from less than 2% between the inner and outer cylinders ($\overline{Nu}_i = 1.699$, $\overline{Nu}_o = 1.732$). On the other hand, when the simulation starts by using the developed flow computed for $Ra = 6000$, the three-dimensional pattern is preserved at the steady state (Figure 7(b)). The three-dimensionality of the flow field is confirmed by the 40%-relative difference between the average Nusselt numbers evaluated on the cylinder walls at $z = A/2$ ($\overline{Nu}_i = 1.612$, $\overline{Nu}_o = 2.253$). Notice however that the average Nusselt number calculated on the entire inner or outer surfaces is only slightly larger than its value for two-dimensional flow ($\approx 4\%$). It can be thus concluded that the heat transfer rate may be evaluated with a reasonable accuracy from results of 2D-simulations. Finally, it is worth noting that a similar three-dimensional flow pattern was observed in the experimental work by Grigull and Hauf [15] for $R = 1.64$ and $Ra = 13{,}160$. To explain their result, it is suggested that the increase in the temperature difference applied between the cylinder surfaces required to reach $Ra = 13{,}160$ was slow, so that the three-dimensional pattern achieved in the instability region was preserved.

According to Grigull and Hauf [15], reversal transitions to two-dimensional flows occur above $Ra = 21{,}000$, for $1.3 \le R \le 6.3$. This Rayleigh number value is close to the instability threshold Ra_{c_3} (Figure 5) at which three-dimensional oscillatory perturbations are predicted. To study the instability of the two-dimensional flow above Ra_{c_3}, numerical simulations were carried out for $R = 1.7$ and $Ra = 22{,}000$, for various axial aspect ratios. For small aspect ratio ($A = 6$), the flow converges towards a steady flow with a structure mainly two-dimensional. This solution contradicts the stability analysis but agrees with the two-dimensional flow observed experimentally by Grigull and Hauf [15] for $Ra > 21{,}000$ and $1.3 \le R \le 6.3$. For a larger aspect ratio ($A = 20$), the flow was oscillatory with a frequency equal to the frequency predicted by

www.pphmj.com

the linear stability analysis at the threshold Ra_{c_3}. Nevertheless, the flow seems to remain essentially two-dimensional with the largest axial components of velocity located near the end walls (Figure 8). For example, the streamfunctions, illustrated by the fluid particle tracking in the core region and at a fixed time, look like those of two-dimensional patterns. The three-dimensional behaviour of the flow consists in weak spatial oscillations associated with steady and travelling waves within the core region and close to the lateral walls of the annular space, respectively [26]. The wavenumbers predicted numerically and those from the stability analysis are in good agreement. The simulations for two very different aspect ratios showed that the flows were mainly characterized by 2D-flow patterns in the core region of the annulus. Thus, these results may be considered in qualitative agreement with the experimental observations by Grigull and Hauf [15] for $Ra > 21{,}000$ and $1.3 \leq R \leq 6.3$, at least near the instability threshold.

For large gap annuli, the transition at Ra_{c_4} is well represented by the marginal curve plotted by Powe et al. [28] in their stability chart. Whereas the critical parameters are in qualitative concordance, the steady nature of the transition predicted by the linear stability analysis does not match the flow oscillatory regime observed experimentally [2, 3, 18] and numerically [25]. The bifurcation at Ra_{c_4} is therefore probably subcritical. In both cases, linear perturbations and flows break the symmetry of the basic two-cellular solution. The flow consists in an unsteady thermal plume in each (r, θ)-plane. For $Ra = 130{,}000$, $R = 2.4$ and $A = 6$, the thermal plume periodically oscillates and forms a steady axial wave.

www.pphmj.com

V. Conclusion

Natural convection in air-filled horizontal annuli has been investigated for radius ratios and Rayleigh numbers in the ranges $1.2 \leq R \leq 3$ and $Ra < 150{,}000$. Two-dimensional studies of flows as a function of Ra and R have clearly highlighted the parameter sets for which two or three possible solutions exist, depending on the initial conditions. Linear

stability analyses have shown that all the flow transitions are induced by three-dimensional disturbances. The following asymptotic states were exhibited as a function of the radius ratio: for narrow-gap annuli ($R < 1.5$), transverse steady rolls are amplified beyond $Ra_c \approx 2000$; multiple transitions occur for two-dimensional flows in moderate-gap annuli ($1.5 < R < 2$); for large-gap annuli with $R > 2$ oscillatory disturbances are amplified for $2 < R < 2.24$ and $Ra = \mathcal{O}(10^4)$ while steady symmetrical breaking disturbances are amplified for $R > 2.24$ and $Ra = \mathcal{O}(10^5)$. 3D-numerical simulations have confirmed these findings. For moderate gap annuli, the steady flow states lying in the new stable region discussed in the present paper depend on the initial conditions applied to simulate the transient regime by using a time-marching procedure. Finally, the onset of instabilities are delayed for small axial aspect ratios.

Acknowledgements

Computational facilities were made available by the Institut de Développement et des Ressources en Informatique Scientifique (I. D. R. I. S), the CNRS Computer Centre in Orsay, France, under research projects nos. 031265-051265.

www.rphnt.com

References

[1] W. Beckmann, ForschHft. Ver. Dt. Ing. 2 (1931), 165.

[2] E. Bishop and C. Carley, Proc. Heat Trans. Fluid Mech. Inst. (1966), 63-78.

[3] E. Bishop, C. Carley, and R. Powe, Int. J. Heat Mass Trans. 11 (1968), 1741.

[4] P. Cadiou, G. Desrayaud and G. Lauriat, ASME J. Heat Trans. 120 (1998), 1019.

[5] M. C. Charrier-Mojtabi, A. Mojtabi and J. Caltagirone, J. Heat Trans. 101 (1979), 171.

[6] A. Cheddadi, J. Caltagirone, A. Mojtabi and K. Vafai, J. Heat Trans. 114 (1992), 99.

[7] E. Chénier, G. Petrone and G. Lauriat, Proc. of the Annual Congrès Francais de Thermique 14 (2006), 241.

[8] J. Choi and M. U. Kim, Int. J. Heat Mass Trans. 36 (1993), 4173.

[9] J. Chung, C. Kim, H. Yoo and J. Lee, Num. Heat Transfer-Part A 36 (1999), 291.

[10] G. Desrayaud, G. Lauriat and P. Cadiou, Int. J. Heat Fluid Flow 21 (2000), 65.

[11] M. Dyko, K. Vafai and A. Mojtabi, J. Fluid Mech. 381 (1999), 27.

[12] M. Dyko and K. Vafai, J. Fluid Mech. 445 (2001), 1.

[13] M. Dyko and K. Vafai, Phys. Fluids 14 (2002), 1291.

[14] K. Goda, J. Comput. Phys. 30 (1979), 76.

[15] U. Grigull and W. Hauf, Proc. of the Third Int. Heat Transfer Conference, Paper No. 60, 2 (1966), 182-195.

[16] G. Karniadakis, M. Israeli and S. Orsag, J. Comput. Phys. 97 (1991), 414.

[17] C. Kim and S. Ro, Proc. Int. Heat Transfer Conference 7 (1994), 85-90.

[18] G. Labonia and G. Guj, J. Fluid Mech. 375 (1998), 179.

[19] C. Mamun and L. Tuckerman, Phys. Fluids 7 (1995), 80.

[20] J. Mizushima and S. Hayashi, Phys. Fluids 13 (2001), 99.

[21] J. Mizushima, S. Hayashi and T. Adachi, Int. J. Heat Mass Trans. 44 (2001), 1249.

[22] A. Mojtabi and J. P. Caltagirone, J. de Mécanique 18 (1979), 225.

[23] A. Mojtabi and J. P. Caltagirone, Phys. Fluids 22 (1979), 1208.

[24] G. Petrone, E. Chénier and G. Lauriat, Int. J. Heat Mass Trans. 47 (2004), 3889.

[25] G. Petrone, Ph.D. Thesis, University of Marne-la-Vallée, 2004.

[26] G. Petrone, E. Chénier and G. Lauriat, Int. J. Heat Mass Trans. 49 (2006), 1231.

[27] G. Petrone, E. Chénier and G. Lauriat, Phys. Fluids (submitted).

[28] R. Powe, C. Carley and E. Bishop, Trans. ASME C: J. Heat Trans. 91 (1969), 310.

[29] R. Powe, C. Carley and S. Carruth, Trans. ASME C: J. Heat Trans. 93 (1971), 210.

[30] Y. Rao, Y. Miki, K. Fukuda, Y. Takata and S. Hasegawa, Int. J. Heat Mass Trans. 28 (1985), 705.

[31] J. Yoo, Int. J. Heat Fluid Flow 17 (1996), 587.

[32] J. Yoo, Int. J. Heat Mass Trans. 46 (2003), 2499.

www.pphmj.com

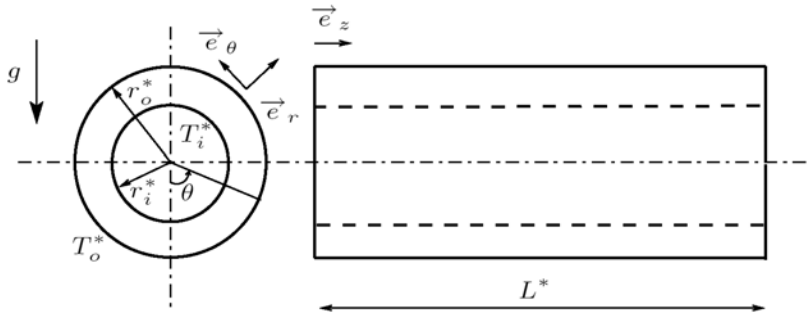

Figure 1. Geometry.

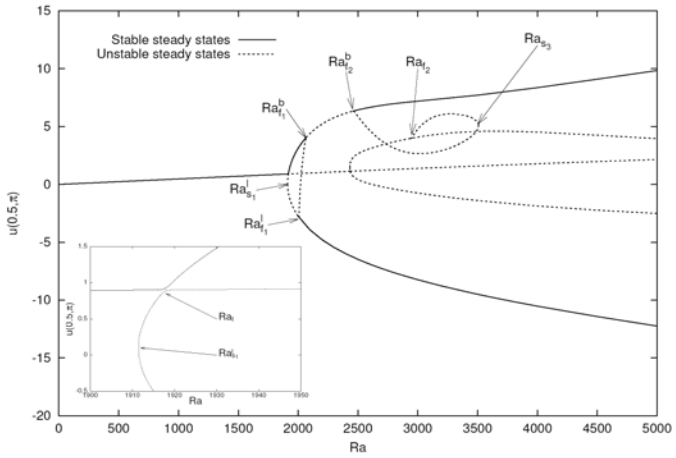

Figure 2. Bifurcation diagram and enlargement for $Ra \in [1900; 1950]$: $u(0.5, \pi)$ versus Ra. Continuous (resp. dashed) lines stand for branches of stable (resp. unstable) solutions, [24].

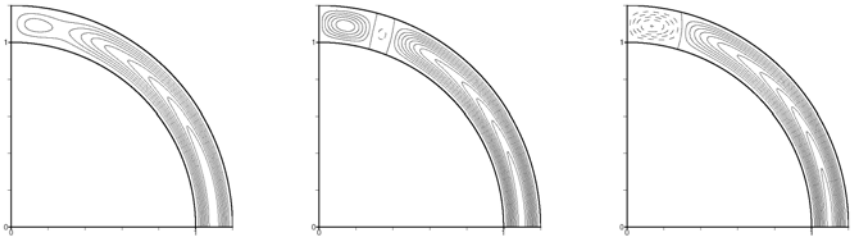

(a) c^+C^+ pattern at $Ra = 2000$, $(0; 4.5, [0.5])$

(b) $C^+C^-C^+$ pattern at $Ra = 2500$, $(-1; 6, [0.5])$

(c) C^-C^+ pattern at $Ra = 5000$, $(-5; 12, [1])$

Figure 3. Streamlines of steady states lying on the (a), (b), basic-branch and (c) lower branch of the bifurcation diagram (Figure 2), [24].

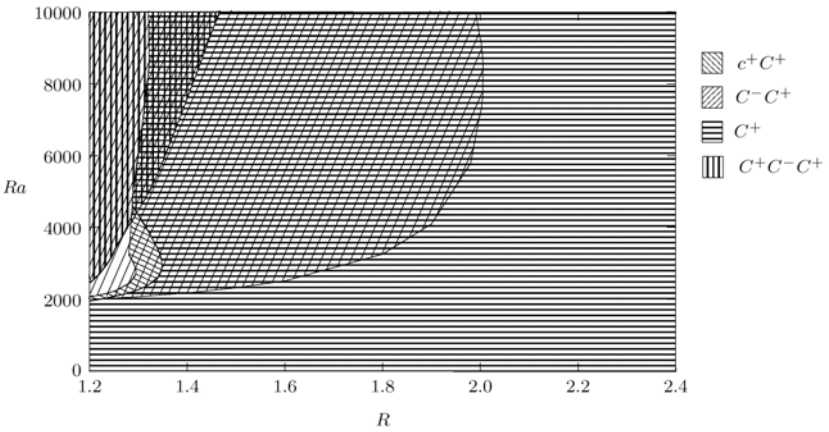

Figure 4. Two-dimensional stable flow patterns in the (R, Ra) plane, [24].

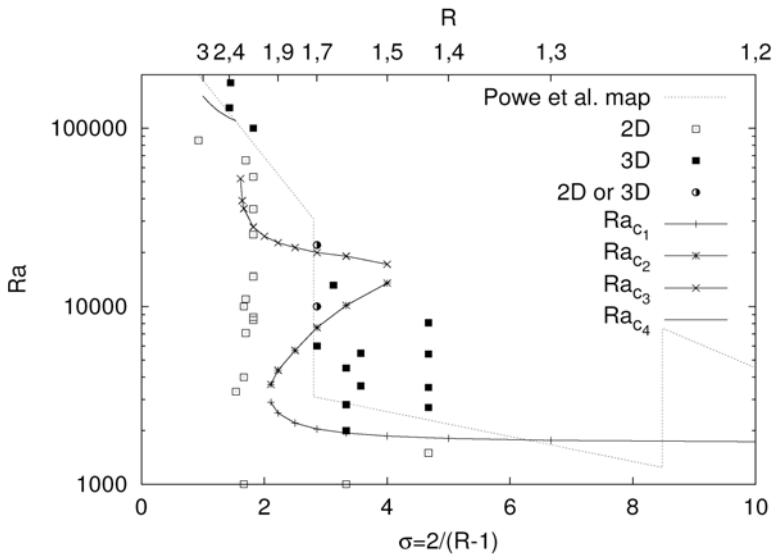

Figure 5. Stability thresholds, Ra_c, as a function of σ or R; comparisons with the literature [4-7, 9, 23, 24, 27, 32].

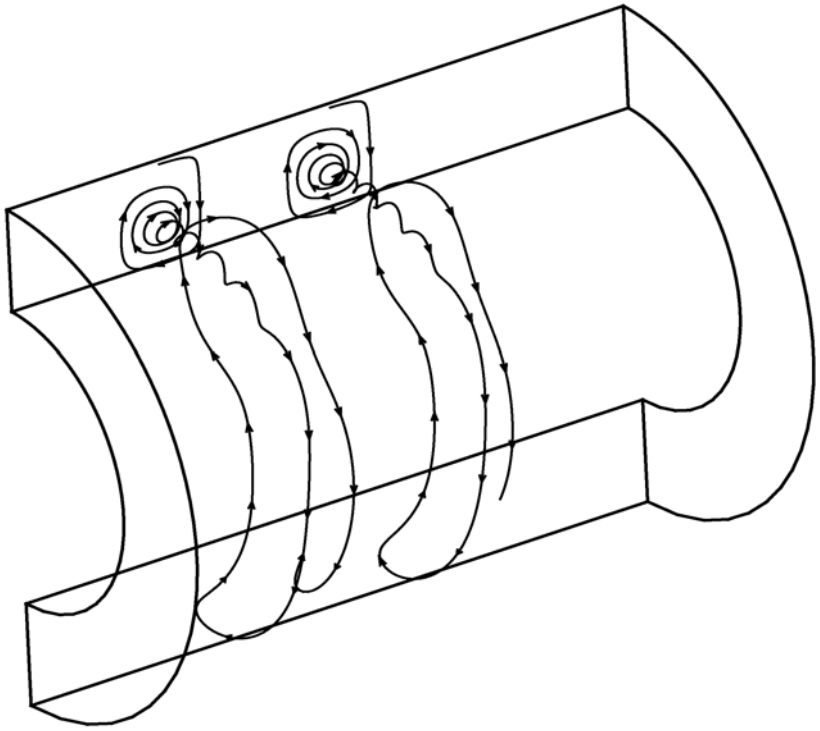

Figure 6. Two streak lines for $R = 1.7$, $A = 6$ and $Ra = 6 \cdot 10^3$, [26].

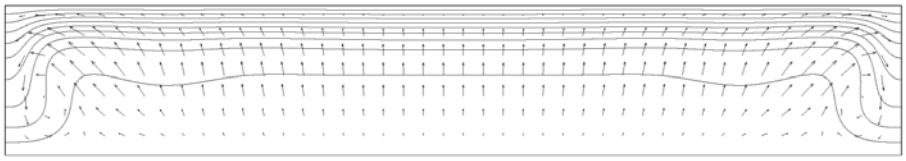

(a) Fluid flow initialized by rest conditions

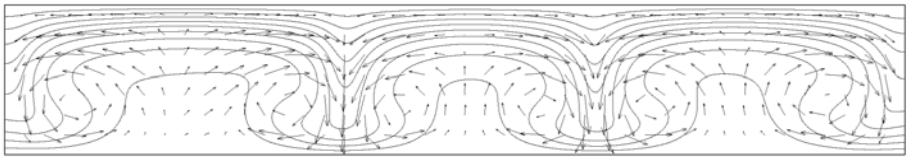

(b) Fluid flow initialized by the 3D-flow at $Ra = 6 \cdot 10^3$

Figure 7. Isotherms and velocity vectors in the vertical (r, z) top section achieved by two initial conditions, for $R = 1.7$, $A = 6$ and $Ra = 10^4$, [26].

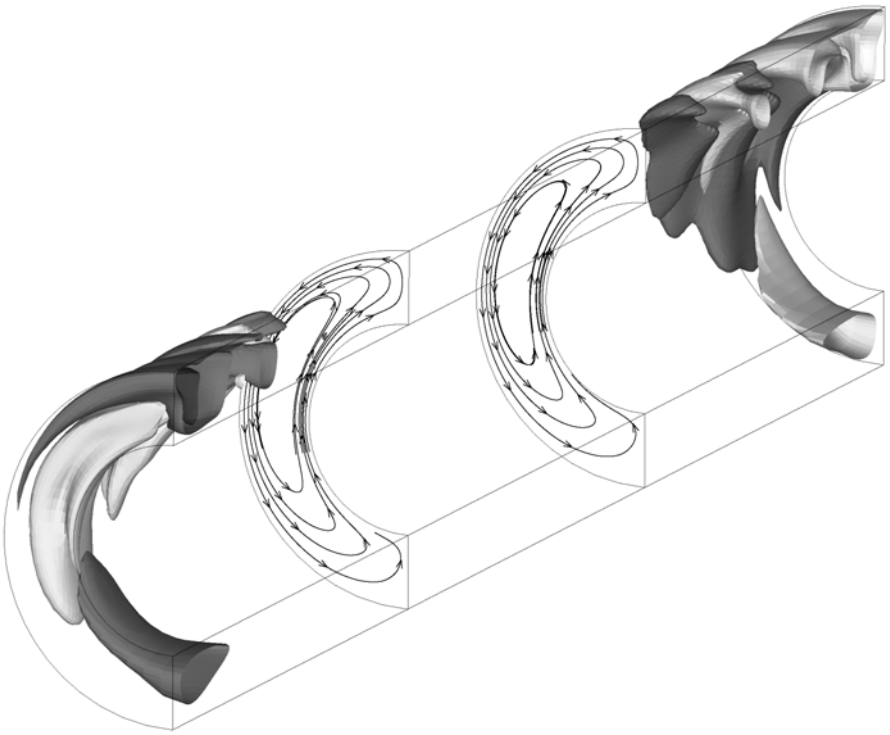

Figure 8. Isosurfaces of the axial component of the velocity and streak lines for $R = 1.7$, $A = 20$ and $Ra = 22{,}000$, [26].

■